Wiley Modelling and Simulation in Engineering Volume 2025, Article ID 9939388, 19 pages https://doi.org/10.1155/mse/9939388



Research Article

Minimizing Aero-Optic Effects on UAV Camera Systems: A Numerical and Design Approach

Ali Esmaeili D, Mohammad Hossein Moghimi Esfandabadi D, Kamyab Karbasishargh, and Mahyar Najafian

Mechanical Engineering Department, Engineerring Faculty, Ferdowsi University of Mashhad, Mashhad, Iran

Correspondence should be addressed to Ali Esmaeili; aliesmaeili@ferdowsi.um.ac.ir

Received 22 March 2025; Revised 27 August 2025; Accepted 9 September 2025

Academic Editor: Franco Ramírez

Copyright © 2025 Ali Esmaeili et al. Modelling and Simulation in Engineering published by John Wiley & Sons Ltd. This is an open access article under the terms of the Creative Commons Attribution License, which permits use, distribution and reproduction in any medium, provided the original work is properly cited.

This article delves into the challenges of aero-optics, specifically focusing on how thermal and density variations in fluid flow around UAV-mounted cameras can disrupt imaging accuracy. Turbulent eddies created by the camera enclosure cause light refraction, affecting camera positioning, trajectory, and image quality. To address these issues, this interdisciplinary study explores the fusion of aerodynamics and optics, investigating diverse camera enclosure designs and key parameters. A comprehensive analysis of the causes and consequences of aero-optic phenomena on imaging systems is presented. The Gladstone–Dale equation is harnessed to infer the refractive index from density data, and the fourth-order Runge–Kutta method is employed for ray tracing, uncovering light deviations. Our findings demonstrate a 71% reduction in optical deviation due to exhaust cooling and strategic camera placement on UAVs, significantly improving imaging accuracy. This work highlights the importance of considering aero-optic effects in the design and deployment of UAV camera systems for optimal performance. Uncertainties resulting from mesh resolution, turbulence closure, and modeling assumptions were reflected in the maximum local error between predicted and measured velocities, which was roughly ±10%.

Keywords: aero-optic; computational fluid dynamics; optical aberrations; ray tracking

1. Introduction

Unmanned Aerial Vehicles (UAVs), commonly known as drones, have revolutionized various fields, from aerial photography and surveillance to delivery and precision agriculture [1, 2]. Among their vital tools are imaging systems, enabling crucial tasks like target identification and navigation [3]. However, the performance of these systems can be significantly compromised by aero-optical effects, leading to errors in targeting and potentially jeopardizing the entire mission [4]. Understanding and mitigating these effects is paramount for ensuring the safe and reliable operation of high-speed aerial platforms [5].

1.1. Challenges and Sources of Error. While imaging systems rely on sophisticated software and electronics, their accuracy can be severely hampered by factors beyond purely technical limitations. A key culprit is the complex interplay between

airflows and light. This manifests in several ways, as seen in Table 1:

- Density variations: As light traverses different environments, including air—water interfaces and boundary layers around the drone, its path deviates due to changes in the refractive index [6, 7]. This phenomenon, known as aero-optics, distorts the captured images, compromising crucial information [8].
- Turbulence: High-speed airflows are often turbulent, characterized by chaotic eddies and fluctuations in density and temperature [11]. These turbulent currents distort and scatter light, further degrading image quality and obscuring critical details [4].
- Flow structures: Specific flow structures around the drone, such as those generated by turrets or engine pods, create localized regions of intense aero-optical

Effect	Consequence	Example	References
Density variations	Image blurring-refraction-defocusing	Air-water interface-temperature gradients	Handler et al. [6], Peleg and Moloney [7], Shao et al. [8]
Turbulence	Image jitter-loss of resolution-scattering	Boundary layers-engine wakes	Yang et al. [4], Lynch et al. [5]
Flow structures	Field of view blockage-localized distortion	Turret wakes-wingtip vortices	Tian et al. [9], Ren et al. [10]

TABLE 1: Examples of aero-optical effects and their consequences.

distortion [10]. These areas can effectively blind the imaging system, rendering parts of the field of view unusable [9].

- 1.2. Existing Studies and Mitigation Strategies. Research into aero-optics has intensified in recent years, spurred by the increasing reliance on laser-based systems for various military and civilian applications [10]. Numerous studies have explored diverse approaches, as summarized in Table 2:
 - The relationship between velocity fields and optical distortion: Analyzing velocity structures provides insights into the nature and location of aero-optical effects [14]. Tools like the Reynolds analogy can further predict boundary layer behavior and its impact on imaging [11].
 - Adaptive optics (AO) technologies: AO systems utilize deformable mirrors and wavefront sensors to actively compensate for atmospheric and aero-optical distortions in real time, significantly improving image quality [12, 13].
 - Numerical simulations and wind tunnel experiments: Computational fluid dynamics (CFD) simulations and wind tunnel tests are crucial for studying complex flow structures and their interactions with light [4, 5]. These tools help optimize turret designs and develop strategies for minimizing distortion [9].

1.3. Challenges and Opportunities. Despite significant progress, several challenges remain. Accurately modeling and predicting complex 3D turbulent flows around drones poses a significant hurdle [14]. Additionally, existing AO systems may not be agile enough to handle the rapid fluctuations in high-speed environments [15].

Overcoming these challenges presents exciting opportunities for future research. Advances in machine learning and artificial intelligence hold promise for real-time image restoration and correction, effectively "seeing through" aerooptical distortions [10]. Moreover, machine learning techniques, such as neural networks and deep learning, could provide more adaptive and scalable solutions for predicting aero-optic effects under various operational conditions. Additionally, advances in materials science and microelectromechanical systems (MEMS) could pave the way for faster and more adaptable AO systems specifically tailored for high-speed aerial applications [9]. Recent studies, including the work by Ding et al., have demonstrated that machine learning can effectively predict refraction and scattering of

light in turbulent aerodynamic environments, yielding accurate results and significantly reducing computational costs. The hybridization of CFD with data-driven models could lead to the development of smarter, faster optical beam tracking systems [16].

Zhang et al. in 2024 conducted an experimental and numerical study of images seen by a supersonic optical searcher for Mach 5. The seeker guidance performance was also evaluated by analyzing optical wave distortions, image variations, and other indicators. The results indicate that aerodynamic heating effects can diminish the optical performance of the system and lower the quality of recorded images [17]. Yi et al. in [18] investigated the aeroptical effects of cooling by film cooling in supersonic optical windows. The aim of their work is to analyze challenges such as the effect of aerodynamic heating and airflow turbulence on the quality of light transmission and images at high speeds. They showed that film cooling techniques can reduce aerodynamic heating effects, but they create more complex flows, leading to a decrease in image quality [18]. In 2024, Li et al. proposed a comprehensive flow control method including jet cooling, microvortex generators, and boundary layer suction to reduce optical distortion in optical windows. The results show that this method leads to a 14.7% reduction in optical distortion at Mach Number 3 and a maximum reduction of 20% at Mach Number 5, which helps to improve the image quality in these devices [19].

The article systematically investigates aero-optical effects on UAV-mounted cameras through six sections:

- Introduction highlights the problem of aero-optical distortions caused by turbulent airflow and thermal variations around UAV cameras, which affect imaging accuracy and mission success.
- Governing Equations and Model Definition describes the CFD models, turbulence modeling, boundary conditions, mesh independence, and validation methods used to simulate airflow and density fields near the camera.
- 3. Methodology details the optical modeling using the Gladstone–Dale equation to link refractive index with fluid density and the fourth-order Runge–Kutta method for ray tracing light paths, including interpolation and validation.
- 4. Numerical Simulation explores simulations of active and passive control strategies such as hot/cold fluid jets and geometric changes to study their impact on flow behavior and optical distortions.

Strategy	Approach	Advantages	Disadvantages	References
Adaptive optics (AO)	Real-time correction of wavefront distortions	High-fidelity image restoration, fast response	Complex hardware-high computational cost	Gordeyev and Jumper [12], Lynch et al. [13]
Flow management	Control of airflows around the drone	Reduced distortion at source, passive solutions	May require redesign of components	Yang et al. [4], Gordeyev and Butler [14]
Advanced imaging algorithms	Image restoration and denoising postprocessing	Software flexibility, adaptability	Limited effectiveness for severe distortions	Gordeyev and Jumper [12], Ren et al. [10]
Numerical simulations and wind tunnel experiments	Understanding and optimizing flow structures	Virtual testing of various designs, cost-effective	Limited accuracy at high speeds	Yang et al. [4], Lynch et al. [5]

TABLE 2: Mitigation strategies for aero-optical effects.

- Results and Discussion analyzes aerodynamic and optical parameters, showing that specific design and control measures can significantly reduce aerooptical distortions.
- Conclusion summarizes key findings, including a 71% reduction in optical deviation achieved by exhaust cooling and optimal camera placement, and provides design recommendations to mitigate aero-optic effects in UAV imaging.

2. Governing Equations and Model Definition

Three common solvers exist for calculating the density field using the CFD method, which includes direct numerical simulation (DNS), large eddy simulation (LES), and Reynolds-averaged Navier-Stokes (RANS) equations [20, 21]. Based on the instantaneous governing equations, DNS and LES provide instantaneous flow features that are computationally more expensive than RANS. This study employed the improved delayed detached eddy simulation (IDDES) turbulence model to obtain flow field information in an unstable state. Two reasons led to the selection of this model. The first reason is that small eddies are independent of geometry, and the second reason is that large data is unnecessary in the remote areas of the camera. This means that if the mesh elongation is high, the LES model switches to the K-W-SST turbulence model, resulting in reduced computational cost due to the lengthy mesh in the remote areas of the camera. The study was carried out under specific conditions of standard atmospheric temperature and pressure. The study used a Mach number of 0.5. For this purpose, the velocity profile downstream of the camera in the isolated area was studied. Figure 1 indicates the boundary conditions used for this simulation. Additionally, the study confirms that the jet injection simulation was carried out in a steady state, with ANSYS Fluent used for CFD simulations and ray tracing conducted through MATLAB.

2.1. Boundary Condition. The geometry was considered symmetric from both the left and right sides; at the inlet, total temperature and total pressure were chosen; and for the outlet, the static condition was considered. The lower surface was selected as a solid wall with a specified shear stress equal to zero, and the upper surface was chosen as a solid wall with a no-slip condition. In order to ensure the accuracy of the results

and mesh independence, the profile of the average velocity downstream of the camera (bottom of the camera) was investigated for the number of inlets. The results of investigating the independence of the mesh size are shown in Figure 2. Table 3 presents the sizes of the mesh utilized in the investigation of mesh independence and validation.

2.2. Mesh Independence Study. Finally, in order to investigate the independence of the computational domain, the dimensions of the calculation domain were reduced by 20% and increased by 20%. The independence of the lattice and geometric dimensions was explored. Figure 2 is the comparison of velocity profiles derived using three varying mesh resolutions (fine, medium, and coarse). The figure shows the mesh independence of the results as the velocity profiles approach each other with the refinement of meshes. Figure 3 depicts the effect of varying computational domain sizes (large, medium, and small domains) on the velocity profile. The comparable proximity of the big domain and medium domain curves verifies that the solution is independent of the size of the domain, except that there are some fluctuations in the smallest domain. Figure 4 is a comparison plot of numerical solutions of various turbulence models to experimental data. This figure serves as a verification of good simulations versus experimental measurements agreement with the numerical method. Figures 2, 3, and 4 illustrate the validation and independence from the mesh and dimensions of the computing domain. The calculation of the domain measured 1.1 m upstream from the camera and 1.3 m downstream, with a 0.7-m height and a 10-cm width domain on the upstream side. To evaluate the independence of the mesh, domain dimensions were chosen to be 20% greater and 20% less than those of the main domain in the other two domains.

- 2.3. Fluid Jet Turbulence Model Validation. In addition, the fluid jet turbulence model was validated using the experimental data of Aleyasin et al. [22] in two of the states. Figure 4 illustrates the results for different turbulence models.
- 2.4. Validation and Error Analysis. The computed velocity profiles downstream of the camera were contrasted with the experimental measurements published by Gordeyev et al. [23] in order to verify the numerical accuracy of the CFD simulations. Uncertainties resulting from mesh resolution, turbulence closure, and modeling assumptions were reflected in the maximum local error between predicted

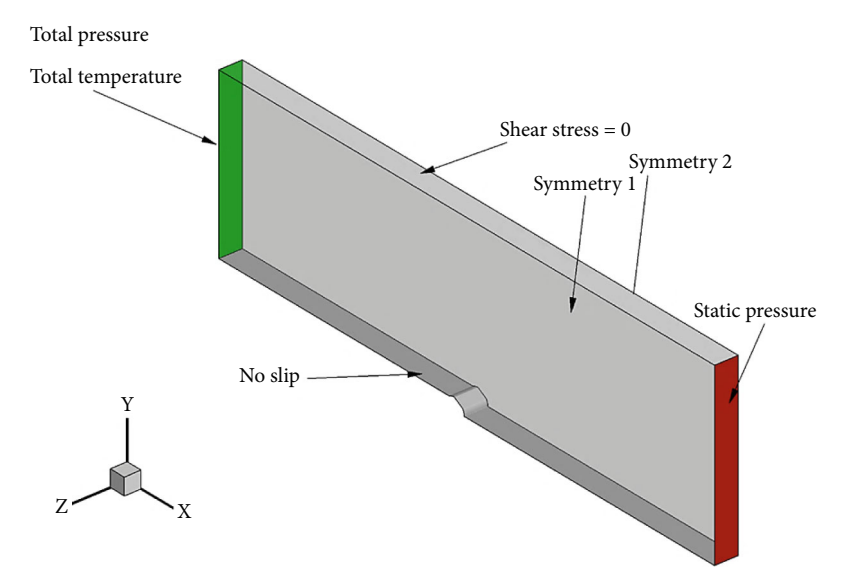


FIGURE 1: Boundary conditions used in the current problem.

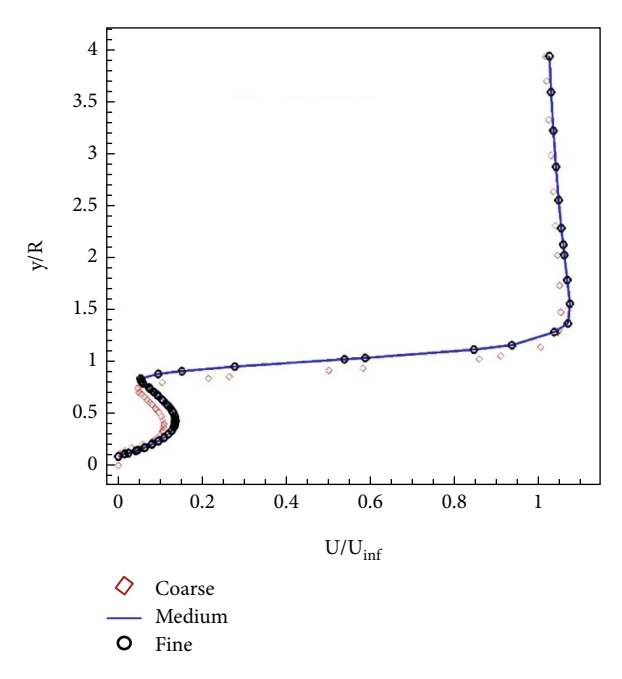


FIGURE 2: Mesh independence study.

TABLE 3: The size of the grids generated for the mesh independence study.

Size	Number of elements	
Coarse	6,114,185	
Medium	7,330,169	
Fine	8,834,979	

and measured velocities, which was roughly $\pm 10\%$. Furthermore, by using a sufficiently small integration step size ($h = 0.5 \, \text{mm}$), numerical errors in the ray tracing algorithm were reduced, leading to a negligible relative tracing error

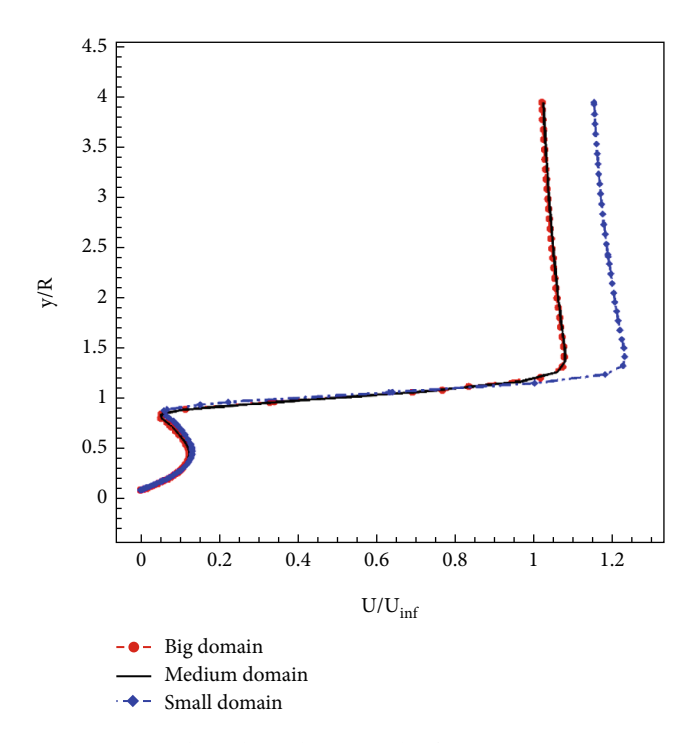


FIGURE 3: Mesh independence study from computation cost viewpoint.

on the order of 10^{-7} . Together, these uncertainty estimates attest to the computational method's dependability and robustness in this investigation. Figure 5 demonstrates the validation of the present numerical simulation with experimental measurements reported by Gordeyev et al. [23].

3. Methodology

Figure 6 shows the schematic of the initial radiation emission position and direction, which is used to track the radiation and extract the outcomes.

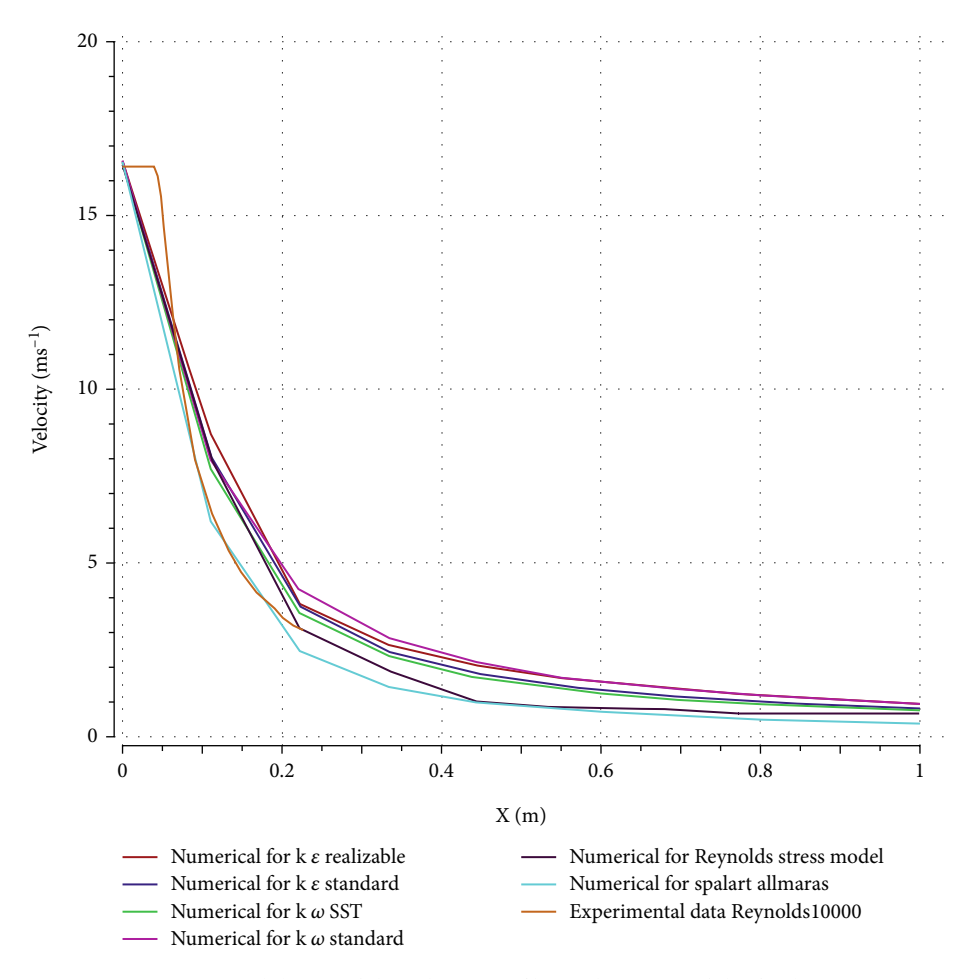


FIGURE 4: Validation of the velocity profile on the center of the fluid jet.

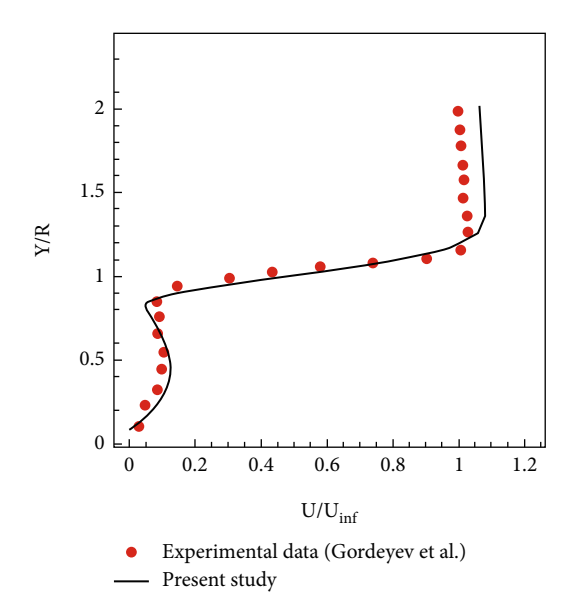


FIGURE 5: Numerical simulation validated with experimental data of Gordeyev et al. [23].

Equation (1), known as the Gladstone–Dale equation, establishes a connection between the refractive index (n) of a material and its density (ρ) . It allows for the calculation

of the refractive index field from a given current density field.

Parameters are as follows:

- *n*: the refractive index of the material. It describes how much light bends when it enters the material, with higher values representing greater bending.
- K_{GD}: the Gladstone–Dale constant, a material-specific proportionality constant that links density changes to refractive index changes. It varies depending on the material's composition and structure.
- ρ: the density of the material, typically expressed in kilograms per cubic meter (kg/m³). It represents the mass of the material per unit volume:

$$n = 1 + K_{\rm GD} \rho \tag{1}$$

Equation (2), a fundamental tool for calculating light deviation, describes how light rays bend when traversing a medium with varying refractive index.

Parameters are as follows:

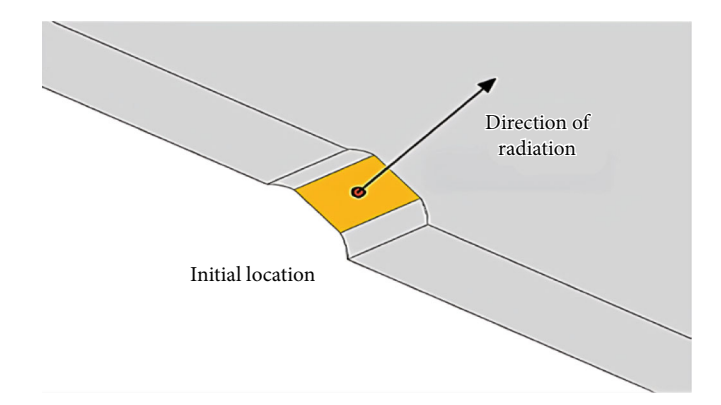


FIGURE 6: Boundary conditions for solving the Runge-Kutta equation (initial position and alignment).

- *d/ds*: the derivative with respect to the arc length (*s*) along the path of the light ray. It measures how quantities change as the ray travels through the medium.
- n(r): the refractive index of the medium at a given position (rr). It captures the medium's ability to bend light, varying from point to point.
- *dr/ds*: the unit tangent vector to the light ray's path, indicating its direction.
- $\nabla n(r)$: the gradient of the refractive index field, representing the direction and magnitude of its spatial variation:

$$\frac{d}{ds}\left(n(n)\frac{dr}{ds}\right) = \nabla n(r) \tag{2}$$

Through the introduction of a novel variable t, defined as the $t = \int ds/dn$, such that dt = ds/n, we achieve a simplification of Equation (1) to Equation (3):

$$\frac{d^2r}{dt^2} = n\nabla n\tag{3}$$

Equation (3) outlines a numerical technique for solving differential equations, specifically employing the fourth-order Runge–Kutta method. This method's full expression is detailed in Equation (4):

Parameters are as follows:

- h: step size used in the numerical integration.
- $r_0(X_0, Y_0, Z_0)$: initial position of the radiation.
- $T_0 = n_0 \nabla n(r_0)$: initial direction of propagation.

• $K_1, L_1, K_2, L_2, K_3, L_3, K_4, L_4$: the intermediate terms used in the Runge–Kutta method are defined in Equations (5), (6), (7), and (8):

$$\{K_1 = T_0 L_1 = D(r_0)\} \tag{5}$$

$$\left\{ K_2 = T_0 + \frac{h}{2} L_1 L_2 = D \left(r_0 + \frac{h}{2} K_1 \right) \right\} \tag{6}$$

$$\left\{ K_3 = T_0 + \frac{h}{2} L_2 L_3 = D \left(r_0 + \frac{h}{2} K_2 \right) \right\} \tag{7}$$

$$\left\{ K_{4} = T_{0} + hL_{3}L_{4} = D(r_{0} + hK_{3}) \right\} \tag{8}$$

When rays collide with a target point at varying angles to the camera's optical axis, the image position at the camera's center is fixed on an imaginary circle. The direction of light emission is determined using the target point. With the initial ray position and direction, the ray can be traced from one location to the next, considering its unique characteristics. This tracking process continues until the entire beam has been traced. To perform this ray tracing method, the refractive index and its gradient are required at every point within the air and optical environment. However, CFD calculations provide discrete refractive indices and gradients based on tetrahedral grid vertices, as depicted in the left section of Figure 7. If the ray's position lies within a quadrilateral grid cell, such as point (*P*) in Figure 7, or on its boundary, the inverse distance interpolation algorithm is employed using a triangular mesh to obtain the refractive index and gradient at that location. First, a triangular mesh is constructed using the Delaney method and initial mesh points. Next, the triangular grid containing point P and its nearest nodes (marked in red) are identified within the mesh. The refractive indices at the three vertices of this triangular grid are used for interpolation.

According to Figure 7 in Delaunay's triangulation method, the refractive index (n) at point P can be calculated by the inverse distance-weighted average interpolation as shown by Equation (9):

$$n = n_1 \varphi_1 + n_2 \varphi_2 + n_3 \varphi_3 \tag{9}$$

where the φ_i coefficients (i = 1, 2, 3) can be calculated by Equation (10):

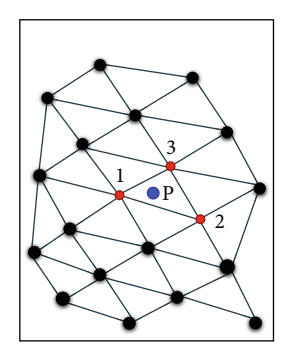


FIGURE 7: A schematic of how to interpolate the value of the refractive index (n) using the vertices of the triangular grid created by Delaunay's triangulation method.

$$\varphi_i = \frac{1/d_i}{(1/d_1) + (1/d_2) + (1/d_3)} \quad (i = 1, 2, 3)$$
 (10)

In Equation (10), d_i (i = 1, 2, 3) is the distances between point P(x, y) and Points 1, 2, and 3 of the triangular domain, which are calculated by Equation (11):

$$d_i = \sqrt{(x - x_i)^2 x + (y - y_i)^2} \quad (i = 1, 2, 3)$$
 (11)

Parameters are as follows:

- d_i : distance between point P and i point in triangle grid.
- (x, y): 2D coordinate of point *P* in triangle grid.
- (x_i, y_i) : 2D coordinate of point *i* in triangle grid.

The triangulation method can also be applied to calculate the refractive index gradient at point *P*. However, because the validation of the numerical ray tracing method is quite complicated, mainly due to the lack of validated empirical data. To investigate the validation of the proposed method, the medium was considered with only radial distribution, which is a solution that exists. The radial distribution of the refractive index of the medium can be expressed by Equation (12):

$$n(x,y) = n_0 \sqrt{1 - \alpha^2 (x^2 + y^2)}$$
 (12)

Parameters are as follows:

- n_0 : refractive index at initial ray position.
- α : radial distribution constant of the medium.

The corresponding Equation (12) can be expressed in Equations (13) and (14):

$$\begin{cases} x = x_0 \cos\left(\frac{n_0 \alpha}{L_0} z\right) \\ + \frac{p_0}{n_0 \alpha} \sin\left(\frac{n_0 \alpha}{L_0} z\right) \\ y = y_0 \cos\left(\frac{n_0 \alpha}{L_0} z\right) \\ + \frac{q_0}{n_0 \alpha} \sin\left(\frac{n_0 \alpha}{L_0} z\right) \end{cases}$$

$$(13)$$

$$\begin{cases} x = x_0 \cos\left(\frac{n_0 \alpha}{L_0} z\right) \\ y = x_0 \sin\left(\frac{n_0 \alpha}{L_0} z\right) \end{cases}$$
 (14)

Parameters are as follows:

- (x_0, y_0) : coordinates of incident ray position.
- L_0 , p_0 , q_0 : initial optical direction cosines.

With the initial condition, Equation (14) simplified into Equation (15):

$$P_0 = 0, X_0 = \frac{q_0}{n_0 \alpha}, Y_0 = 0$$
 (15)

Equation (16) expressed the relative error of ray tracing method:

$$\delta(z) = \frac{\left|r_z - r_z'\right|}{\left|r_z\right|} \tag{16}$$

Parameters are as follows:

- r_z : computational ray position obtained from ray tracing method.
- r'_z : actual ray position from Equation (14) at z plane [23].

In order to verify the accuracy of the method, the refractive index parameter in Equation (12) assumed by $n_0 = 1.5$, $\alpha = 0.01$ [21]. The incident angle of ray was considered 0° and 60°, thus the initial optical direction cosine calculated from Equation (17). Also, the initial position in Equation (18)

$$p_0 = n_0 \sin 60^{\circ}$$

 $q_0 = n_0 \cos 0^{\circ} \cos 60^{\circ}$
 $L_0 = n_0 \sin 60^{\circ}$ (17)

$$x_0 = \frac{\cos 60^\circ}{\alpha}, y_0 = 0, z_0 = 0$$
 (18)

In order to investigate the independency of the ray tracing step size (h), we utilized the same scope of step as previous research [21] was considered. The research indicate that an error caused by the step size (h) is negligible when h is equal to $0.5 \, \text{mm}$.

Figure 8 illustrates a comparison between the analytical solution ray path and the path obtained by a numerical solution (ray tracing method) with a step size of h = 2 mm. The computational curve of ray tracing by numerical simulation corresponds accurately to the actual curve acquired from the analytical solution. In this case, the relative tracing error is 10^{-7} , and the axial movement of the ray (z-direction) has reached 10,000 mm.

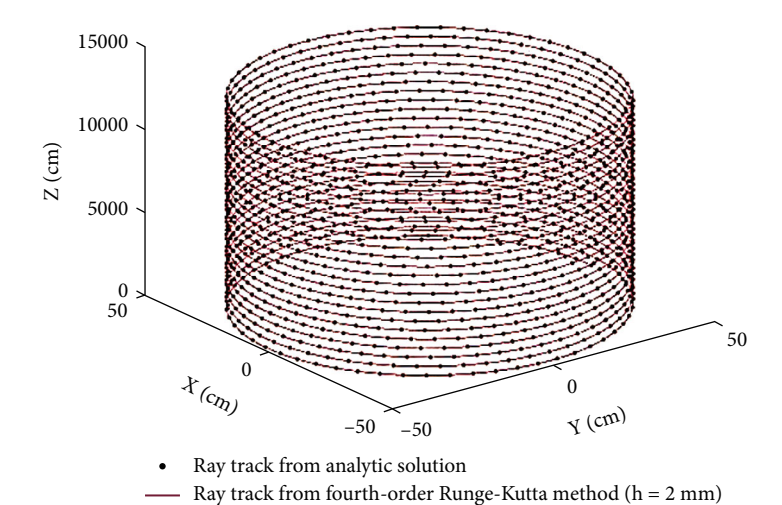


FIGURE 8: Validation of ray tracing with analytical solution.

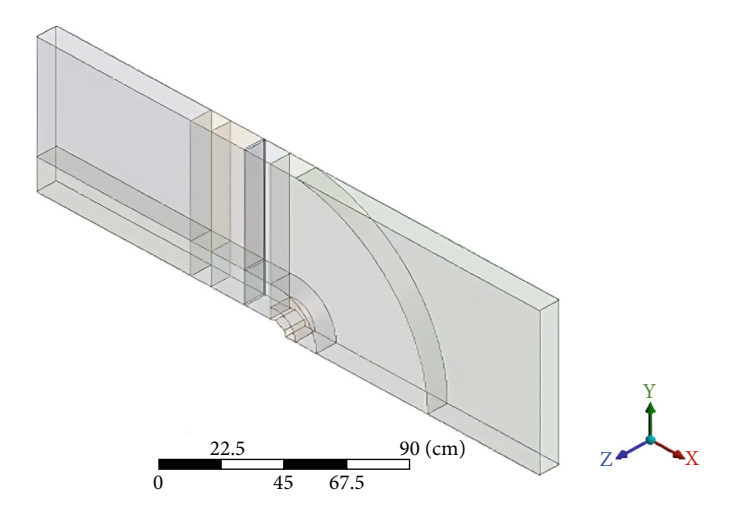


Figure 9: Isometric view of the geometry created based on the experimental research of [12].

4. Numerical Simulation

This section explores and justifies the different types of active and passive control methods employed for investigating fluid dynamics in relation to aero-optic effects, refractive index, and its gradient. We explore the impact of several parameters, including the following:

- i. Hot wall effect simulates the heat flux from engine exhaust in helicopters and airplanes.
- ii. Hot and cold fluid jets mimic hot engine gases and cooled exhaust of stealth aircraft engines, respectively. These models utilize a valve positioned 12 cm upstream of the camera with a length of 0.01 m and a mass flow rate of 0.1 kg/s. Inlet temperatures for hot and cold jets are set at 600 and 298 K, respectively [12].
- iii. Geometrical effects investigate the influence of camera and subsonic flow configurations. The initial analysis establishes a baseline condition matching

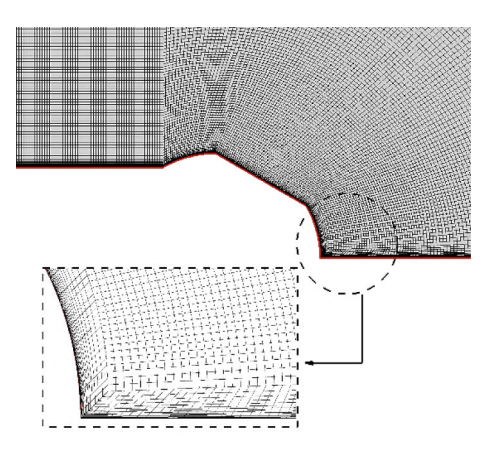


FIGURE 10: The grid used in flow computations.

the geometry used in experimental research. A numerical simulation under these conditions replicates the experimental setup, and the velocity profile downstream of the camera is compared with the actual data shown in Figures 9 and 10. Further

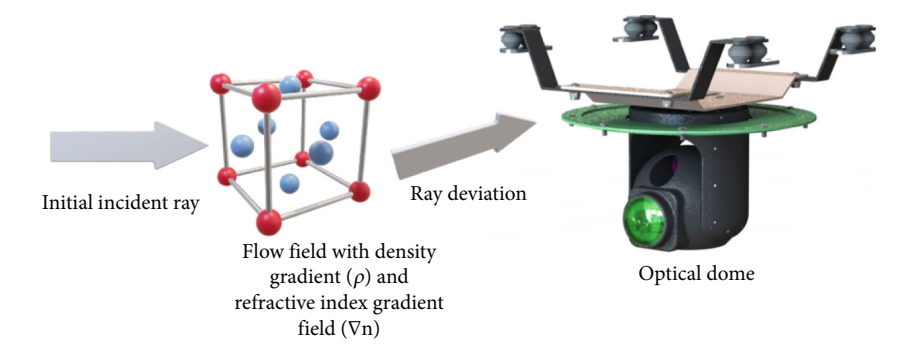


FIGURE 11: Optical ray deviation in flow fields with density and refractive index gradients.

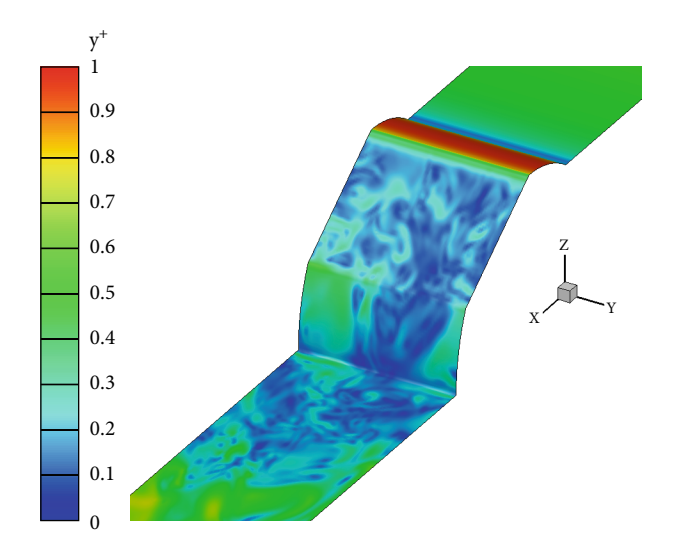


Figure 12: y + contour on the surface of the wall.

simulations then explore optical deviations under various conditions:

- Camera geometry examines the influence of upstream and downstream features, including roughness [23].
- Thermal flux models the engine wall's heat output affecting the exhaust flow [13].
- Hot jet and cooling fluid jet simulate exhaust gases and cooled emissions, respectively, for a cool liquid jet stealth drone [12].
- Hot wall mode models a hot surface 25 cm upstream of the camera, 10 cm long, emitting a thermal flux of 100 kW/m² [13].

Figure 11 illustrates the process by which an initial incident ray interacts with a flow field exhibiting both density gradients (ρ) and refractive index gradients (∇n) , resulting in the deviation of the ray's path. As depicted, the ray first enters a region where variations in fluid density and refractive index alter its trajectory, a phenomenon critical in the study of optical diagnostics for fluid dynamics. The altered ray is then detected by an optical dome equipped with

advanced sensors, enabling precise measurement and analysis of these deviations. This setup is essential for visualizing and quantifying complex flow behaviors in experimental and CFD research.

5. Results and Discussion

As previously established, an aerodynamic field surrounding the camera is responsible for this phenomenon. We will therefore first delve into the nature of this aerodynamic field, followed by an examination of the resulting optical aberrations. Figure 12 depicts the y+ parameter contour on the wall surface. Notably, this variable maintains a value of approximately one across all wall sections, which is crucial for ensuring accurate results when employing the $k-\omega$ SST model.

Figure 13 presents the velocity measurements for various simulated flow modes. Comparing the base mode (including the camera) to the case with the camera appendage removed upstream reveals a more uniform velocity field and a thinner boundary layer. The hot wall mode upstream of the camera shows an increased velocity in the isolated section. Removing the camera base creates a boundary separating the flow further from the separation zone. The cold jet mode exhibits a long separation zone encompassing the entire camera but reduces the separation area's thickness downstream. This might be due to changes in the cold jet's angle, its tendency to reattach to the wall surface, and its interaction with the isolated section. The hot jet creates a detached zone covering the entire camera. Comparing hot and cold jet flows reveals a significantly higher deviation angle for the cold jet fluid. Notably, cold jet fluids exhibit a greater degree of mixing with the mainstream flow, while unmixed hot jet fluid remains in the upper camera regions. Finally, the velocity magnitude within the separation zone of the hot jet is greater than in other modes.

Figure 14 depicts the static pressure contours, revealing distinct flow patterns across examined modes. While prioritizing static pressure uniformity, all test modes exhibit local pressure dips near the camera appendage due to accelerated flow across its curved surface. Notably, the hot wall condition upstream of the flow shows a pressure drop in the separated flow region, where the maximum pressure nearly matches the baseline state. Interestingly, comparing hot and cold jet conditions upstream discloses further insights. The cold jet case exhibits increased static pressure within

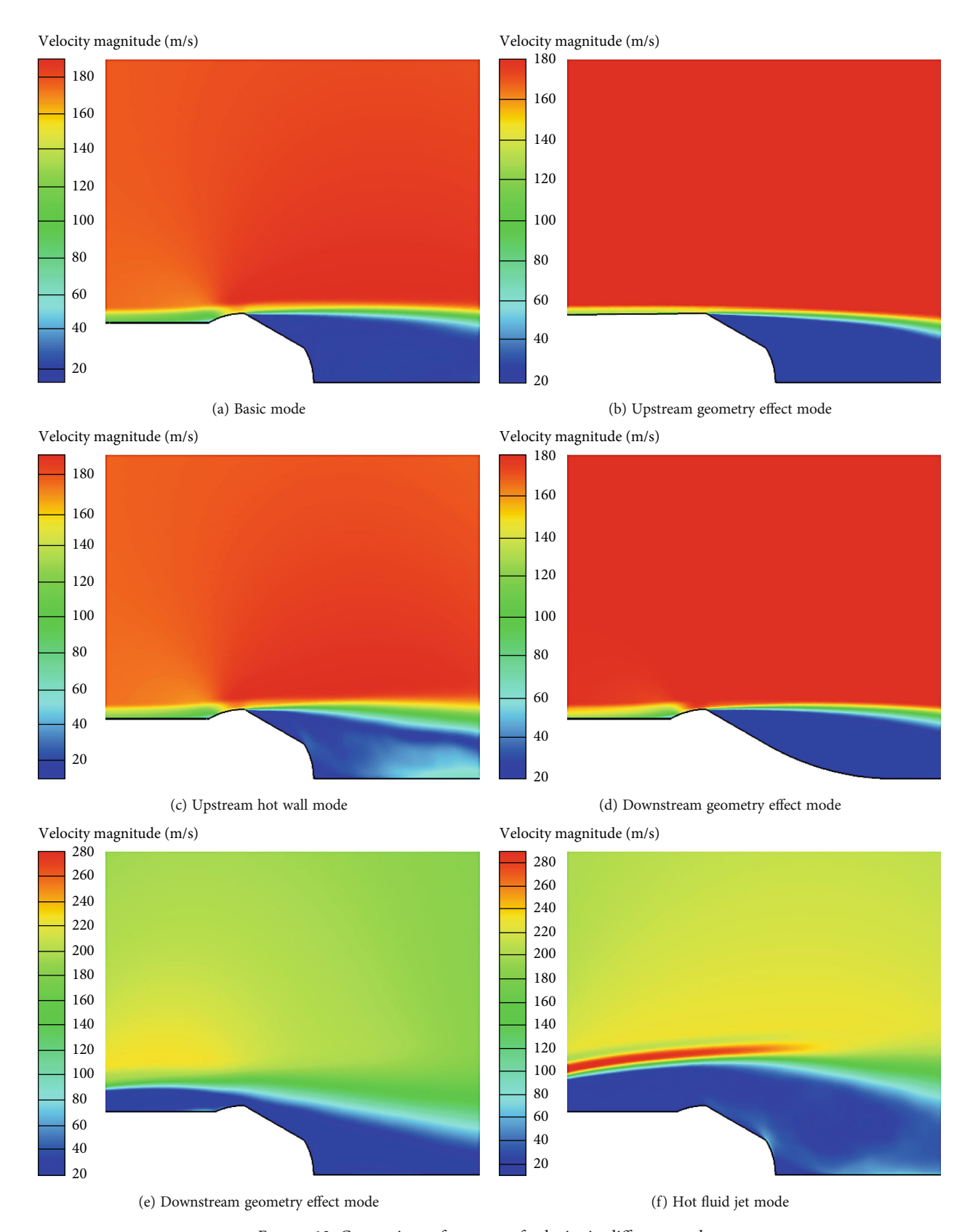


Figure 13: Comparison of contour of velocity in different modes.

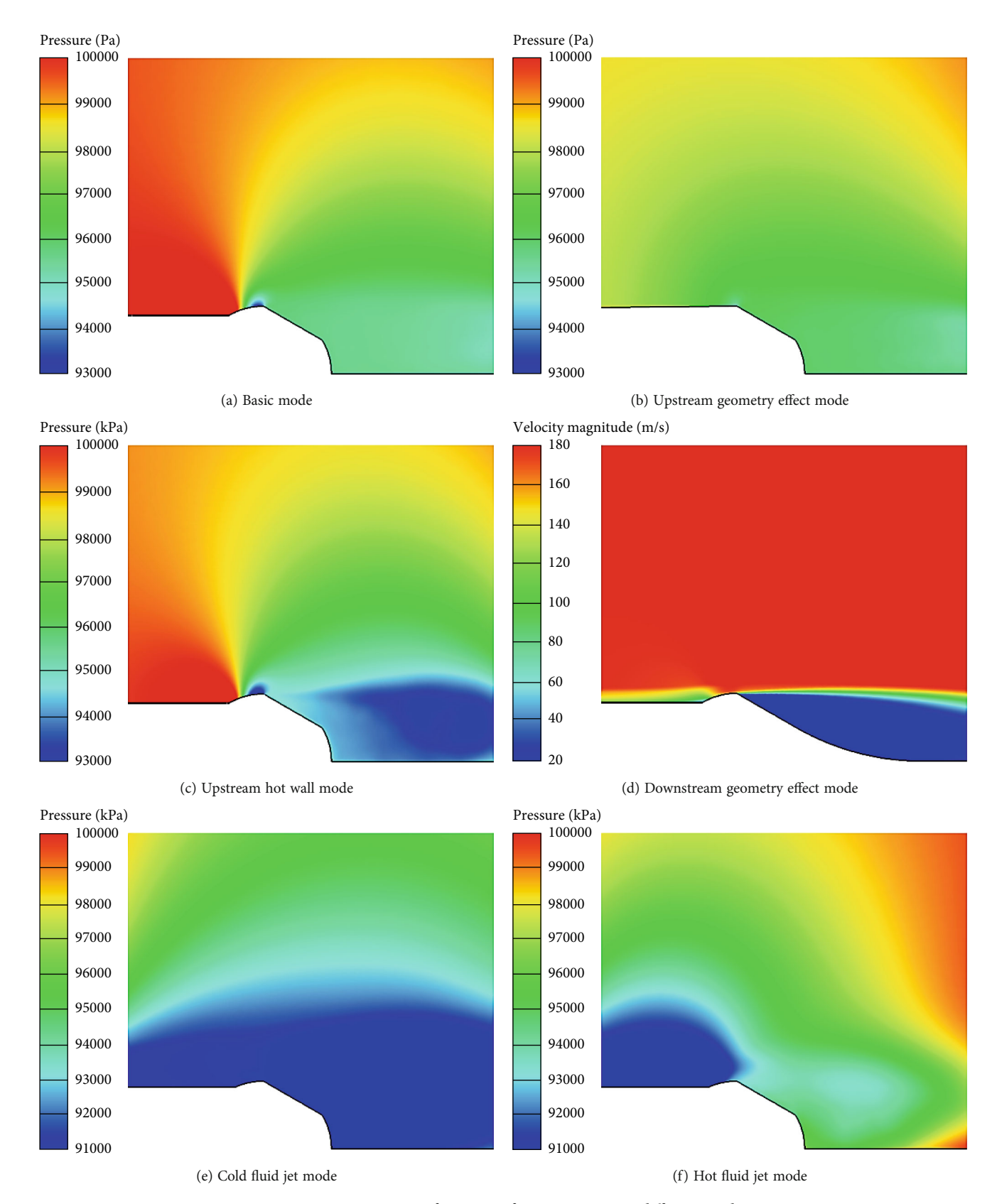


FIGURE 14: Comparison of contour of static pressure in different modes.

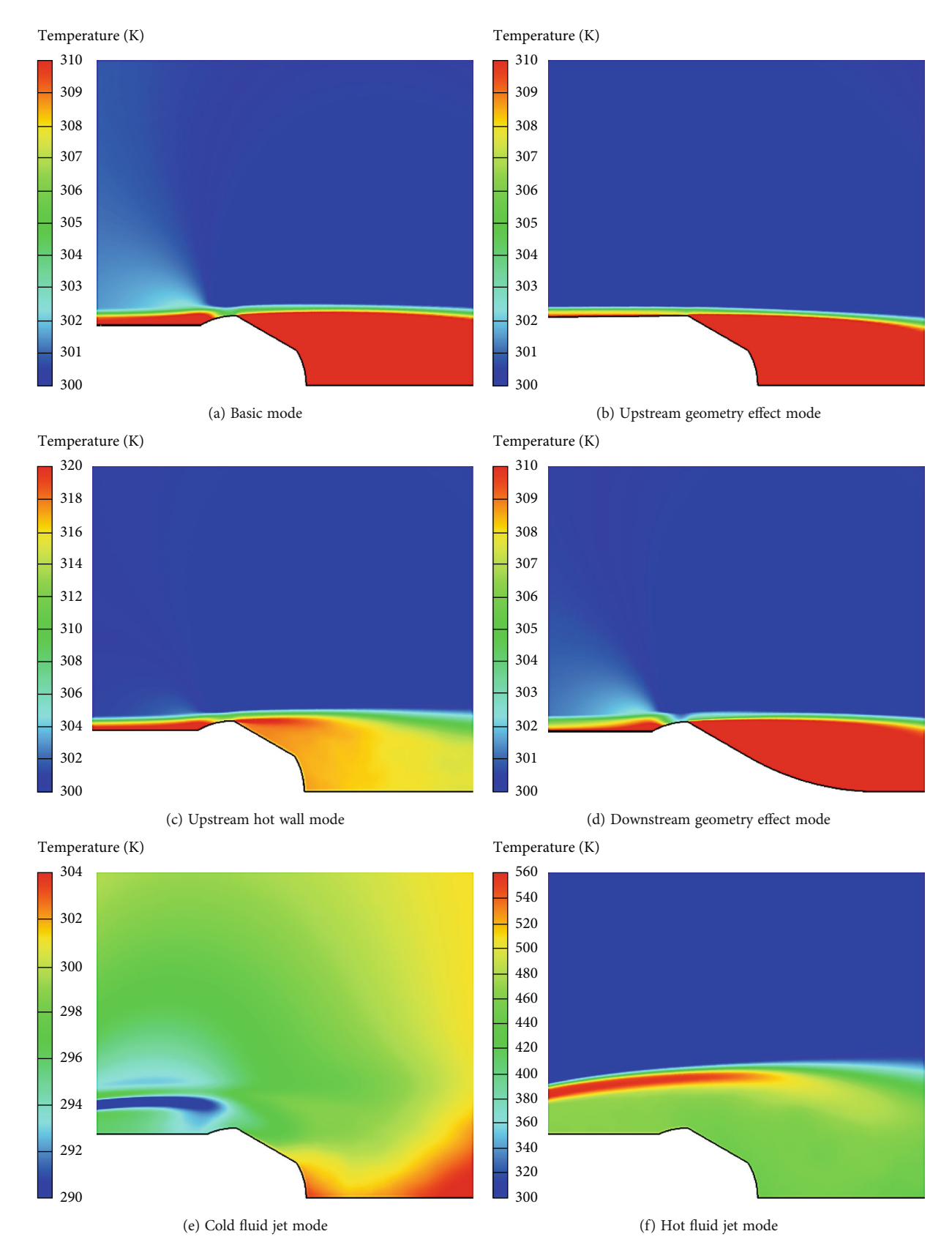


FIGURE 15: Comparison of contour of static temperature in different modes.

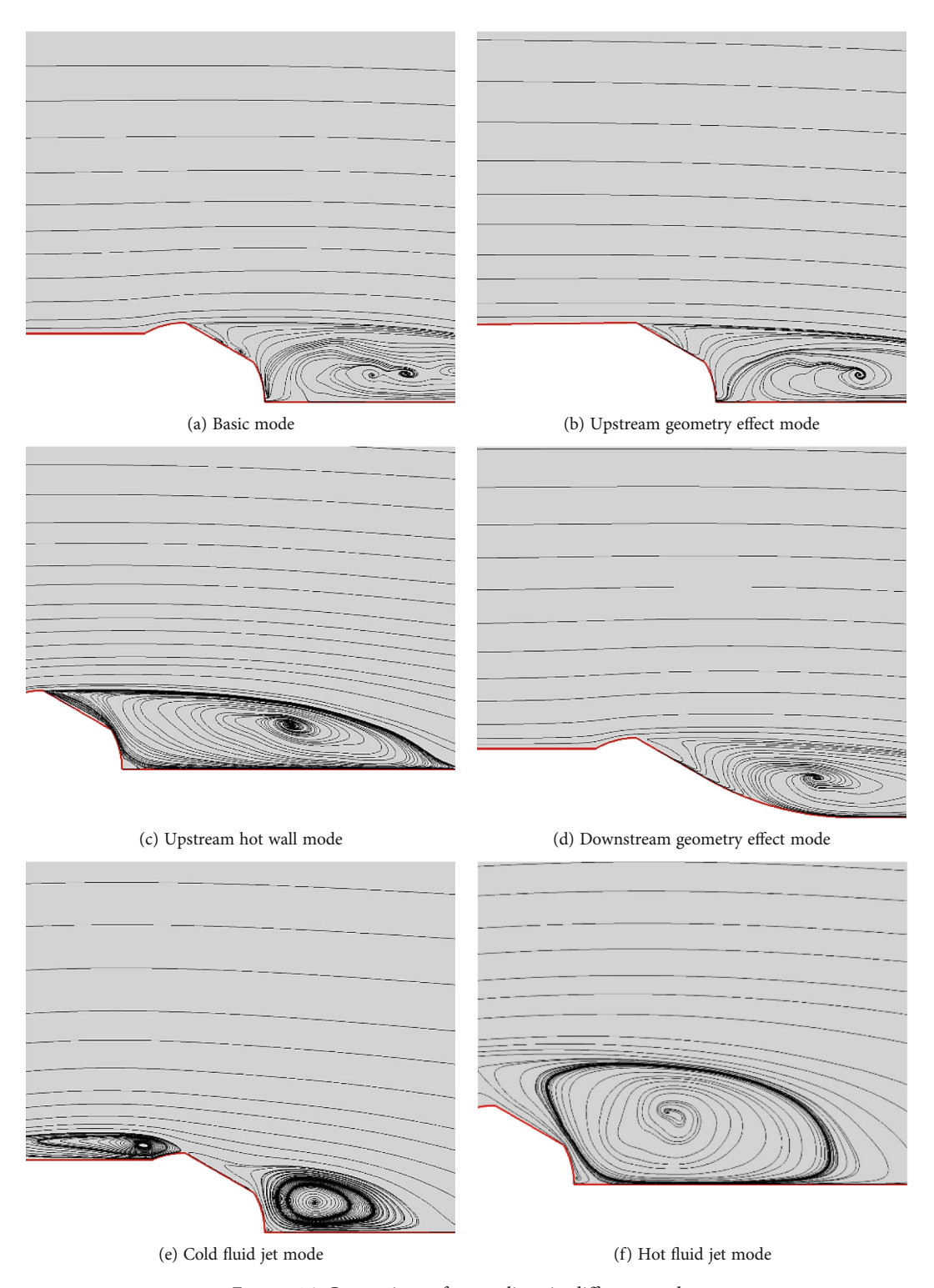
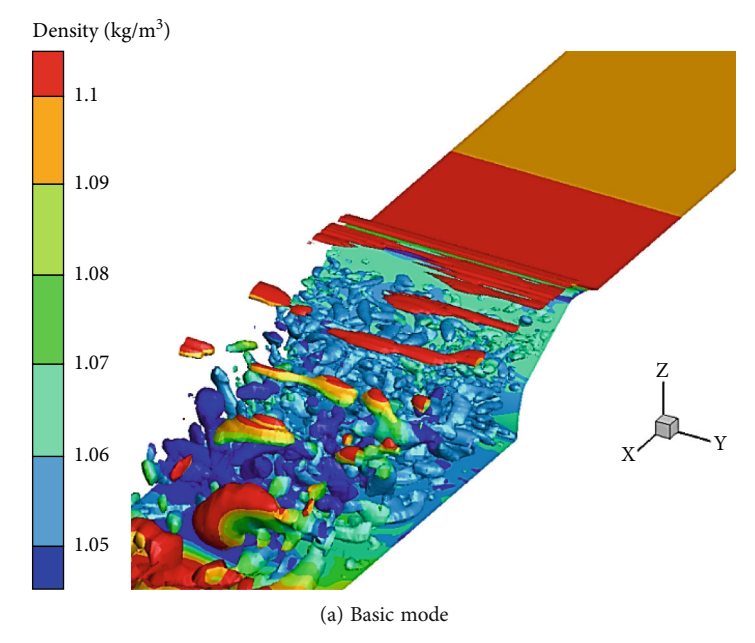


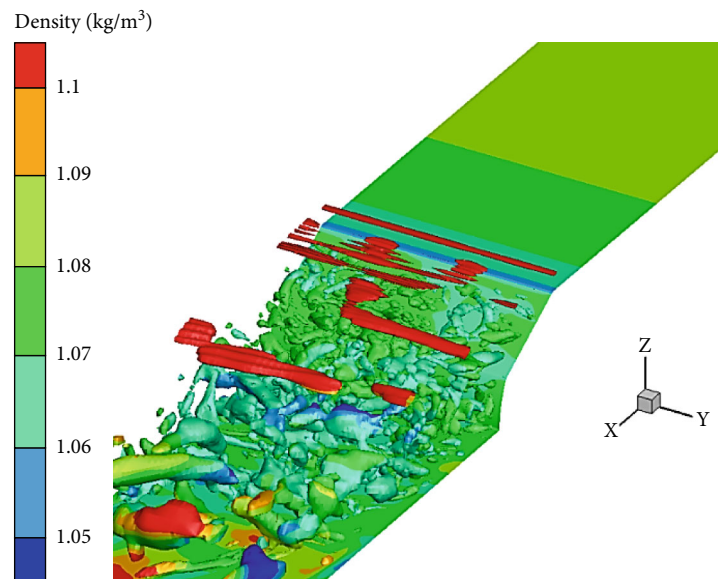
FIGURE 16: Comparison of streamlines in different modes.

the separated flow area, with the minimum pressure now situated upstream of the camera, unlike other test modes. In contrast, the hot jet test displays a static pressure distribution closely resembling the base mode.

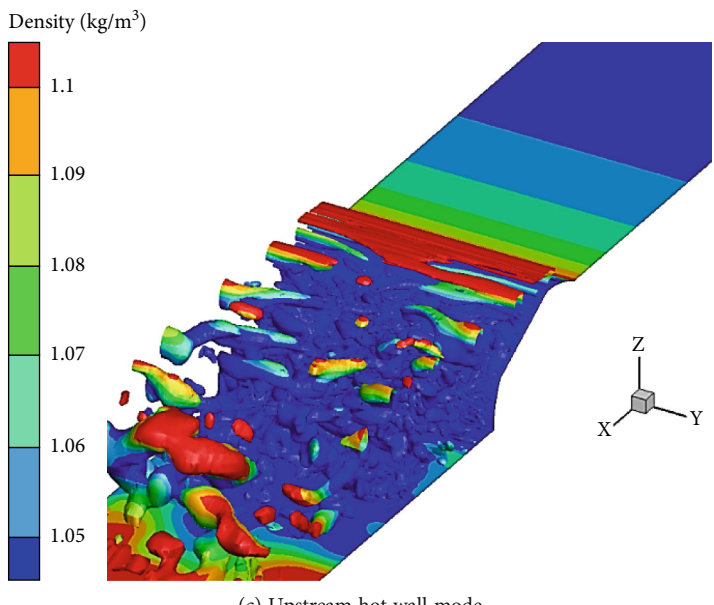
Figure 15 shows the static temperature profiles for various test modes. Among them, only the hot jet state exhibits the maximum static pressure gradient around the camera.

Interestingly, in all modes except those involving jet fluids, the static temperature within the boundary layer and the isolated current section exceeds that of the current's outstream. Further analysis reveals that the hot wall jet upstream has minimal influence on the substantial change in static temperature distribution within the dissolved field. In contrast, the cold jet fluid effectively lowers the temperature in both

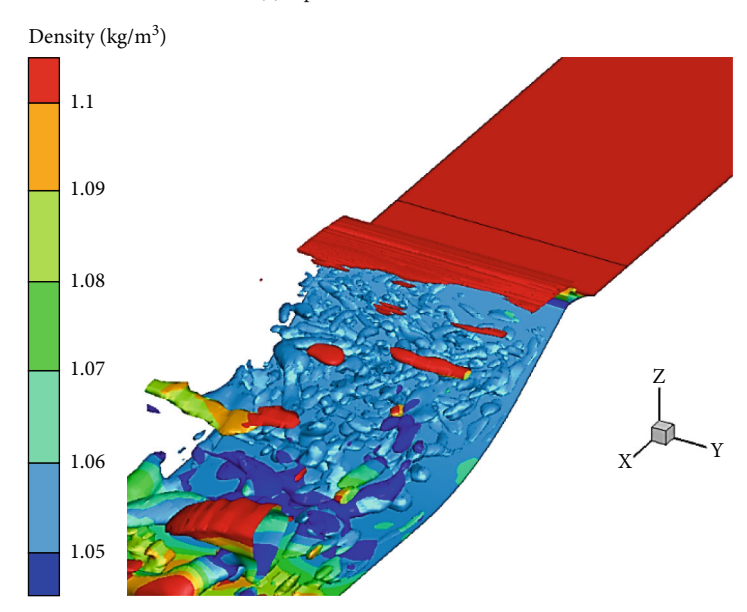




(b) Upstream geometry effect mode Figure 17: Continued.



(c) Upstream hot wall mode



(d) Downstream geometry effect mode

Figure 17: Continued.

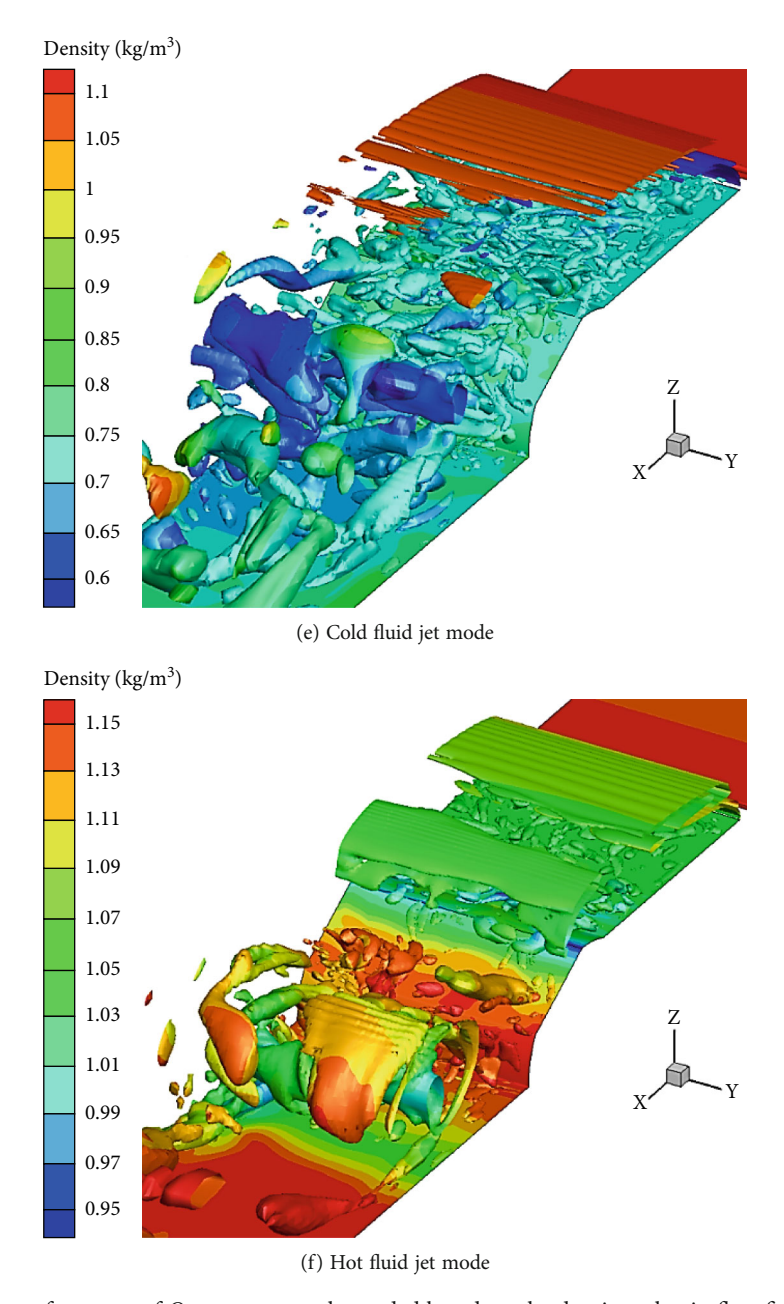


Figure 17: Comparison of contour of Q parameters color-coded based on the density value in flow field in different modes.

the boundary layer and the separated sections. Conversely, the hot fluid jet increases the temperature in these areas, but its core remains stable farther from the jet inlet, creating a significant temperature gradient with the boundary layer flow.

Figure 16 depicts streamlines for various test modes. Comparison of the upstream camera removal mode with its base state reveals nearly identical separation zones and overall vortex formation patterns. In the double hole deletion mode, slight geometric variations in the separation region lead to a slightly different vortex shape. The cold jet mode produces two distinct vortices, located upstream and downstream of the camera, respectively. The vortex size below the camera is smaller in this mode compared to other tested modes. Finally, the hot jet test mode exhibits the larg-

est vortex, which also extends to the highest height above the camera base.

Figure 17 shows the *Q* parameters color-coded based on the density value. It can be observed that the lowest density gradient is related to the downstream camera insertion removal mode test, whereas the maximum density gradient is associated with the hot jet flow.

Modeling the hot wall mode upstream reveals a significant decrease in density within the isolated region compared to other nonjet fluid modes. Notably, the *Q* parameter distribution suggests that the downstream separation area is minimized in cold jet mode, while hot jet mode exhibits a higher concentration of spacers. Table 4 summarizes the optical deviations and errors measured around the camera during tests of different modes. Consistent with the current field

TABLE 4: Angle deviation and vision error caused by angle deviation.

Case	Deflection angle (°)	Position error for 1-km distance
Base case	1e - 03	0.009424
Smooth upwind	6e - 04	0.005222
Smooth down stream	1e - 04	8e – 04
Hot jet	1e - 04	0.16
Cold jet	4e - 03	0.036
Heat flux upwind	3e - 03	0.03

analysis, the hot jet state test showcases the largest optical deviation. Conversely, the downstream camera bezel removal mode demonstrates the minimal deviation. Compared to the baseline, eliminating the upstream bumps and the bezel below the camera reduces optical deviations by 44.58% and 71.54%, respectively.

6. Conclusion and Further Research

6.1. Conclusion

- A 71% reduction in optical deviation was achieved with proper camera placement and the use of exhaust cooling.
- The rate of light refraction and vision error is not significant at Mach 0.5. Nevertheless, the value of this error is predictable and can be utilized to adjust the target position.
- Besides the Mach number, several other factors could impact light refraction and potential deviations.
- The engine's hot exhaust was simulated as an upstream hot jet flowing over the camera, significantly heightening any optical deviations and emphasizing the critical need to design the exhaust system to avoid any flow over the optical apparatus.
- The exhaust in bomber drones is cooled before reaching ambient temperature. The cooled exhaust gas was modeled as a jet-cooled fluid. Jet-cooled fluid around optical systems can cause optical deviations that are detectable with sufficient precision.
- The intensity of optical deflection can be reduced to a visible value if the exhaust output from the engine is cooled before passing over the optical system.
- By removing the upstream camera bump, the optical deviation can be reduced by 44.58%.
- Based on the obtained results, it is better not to position
 the camera in drone parts that are prone to flow separation. For instance, positioning the camera in the initial parts is better than the end parts of the drone. This

TABLE 5: Design checklist for UAV optical systems to minimize aero-optic effects.

Design principle	Explanation/recommended action	
Avoid installation in flow separation areas	Mount the camera in regions with smooth, attached airflow to reduce turbulence and optical distortion.	
Eliminate protrusions	Ensure the camera enclosure is flush with the UAV body; avoid any external bumps or projections to minimize light deviation.	
Cool engine exhaust gases	Cool the hot exhaust before it passes near the camera to reduce density and refractive index variations.	

is because the end parts have a much higher thickness due to the growth of the boundary layer.

- As the projections and other geometric parts of the camera become more level with the body, the harmful effects of air-optical phenomena decrease.
- The hot effects of the body next to the engine were also modeled using a fixed flux wall. While the temperature increases in the vicinity of this wall, the effects will be significantly lower in the nearby parts of the camera. Installing optical systems near these parts may lead to significant optical deviations, so it is advisable to avoid doing so.
- As previously demonstrated, the parameters that affect this phenomenon include heat, secondary flow, and flight speed.
- A checklist of significant design rules for future UAV cam systems: Do not install the enclosure in the flow-separation areas, prefer the configuration with no protrusions, and utilize thermal exhaustion cooling.

To facilitate practical implementation of our findings, a concise design checklist has been developed (Table 5). This checklist summarizes the key considerations for minimizing aero-optic effects on UAV-mounted cameras. By following these principles avoiding flow separation zones, eliminating protrusions, cooling exhaust gases, optimizing camera placement, avoiding hot surfaces, and maintaining smooth body surfaces engineers can significantly reduce optical deviations and improve imaging accuracy in UAV systems.

6.2. Further Research

- i. A detailed study in the supersonic and hypersonic regimes (Mach > 1), where compressibility, shock waves, and aerodynamic heating play supervisory roles in what controls the aero-optical effects, must be considered as a future dimension.
- ii. One of the areas promising future work is the application of artificial intelligence, such as machine learning, in prediction of density gradients, refractive index gradients, and real-time correction of distortion.

Nomenclature

ρ	density of fluid flow [kg/m ³]
$egin{array}{l} ho \ abla n(r) \end{array}$	the gradient of the refractive index field
$r_0(X_0, Y_0, Z_0)$	initial position of the radiation
φ_i coefficients	inverse distance-weighted average
(i = 1, 2, 3)	0 0
(x_i, y_i)	2D coordinate of point i in triangle grid [m]
α	radial distribution constant of the medium
(x_0, y_0) r'_z	coordinates of incident ray position
r_z'	actual ray position at z plane
ν	velocity magnitude of fluid flow [m/s]
T	static temperature of fluid flow [K]
K_{GD}	Gladstone–Dale constant [m³/kg]
h	step size used in the numerical
	integration
T_0	initial direction of propagation
n_0	refractive index at initial ray position
d_i $(i = 1, 2, 3)$	distance between point P and i point
_	in triangle grid [m]
L_0, p_0, q_0	initial optical direction cosines
r_z	computational ray position obtained
	from ray tracing method
<i>y</i> ⁺	parameter related to mesh domain on the wall surface in CFD method
P	static pressure of fluid flow [kPa]
Q	
Q	parameter color-coded based on the density value

*r*efractive index

donaity of fluid flows [1xa/m 3]

Data Availability Statement

The data that support the findings of this study are available from the corresponding author upon reasonable request.

Ethics Statement

The study involving human participants was reviewed and approved by the Ethics Committee of Ferdowsi University of Mashhad.

Consent

Informed consent was obtained from all individual participants.

Conflicts of Interest

The authors declare no conflicts of interest.

Funding

No funding was received for this manuscript.

References

- [1] T. Luo, S. Rao, W. Ma, et al., "YOLOTree-Individual Tree Spatial Positioning and Crown Volume Calculation Using UAV-RGB Imagery and LiDAR Data," *Forests* 15, no. 8 (2024): 1375, https://doi.org/10.3390/f15081375.
- [2] R. Guebsi, S. Mami, and K. Chokmani, "Drones in Precision Agriculture: A Comprehensive Review of Applications, Technologies, and Challenges," *Drones* 8, no. 11 (2024): 686, https://doi.org/10.3390/drones8110686.
- [3] Y. Liu, S. Zhou, H. Wu, W. Han, C. Li, and H. Chen, "Joint Optimization of Autoencoder and Self-Supervised Classifier: Anomaly Detection of Strawberries Using Hyperspectral Imaging," Computers and Electronics in Agriculture 198 (2022): 107007, https://doi.org/10.1016/j.compag.2022.107007.
- [4] B. Yang, Z. Yu, J. Lan, R. Zhang, J. Zhou, and W. Hong, "Digital Beamforming-Based Massive MIMO Transceiver for 5G Millimeter-Wave Communications," *IEEE Transactions on Microwave Theory and Techniques* 66, no. 7 (2018): 3403–3418, https://doi.org/10.1109/TMTT.2018.2829702.
- [5] K. P. Lynch, N. E. Miller, D. R. Guildenbecher, et al., Aero-Optics of Hypersonic Turbulent Boundary Layers (No. SAND2022-13389) (Sandia National Lab. (SNL-NM), 2022).
- [6] R. A. Handler, R. J. Watkins, S. Matt, and K. P. Judd, "Model for the Structure Function Constant for Index of Refraction Fluctuations in Rayleigh-Bénard Turbulence," *Physical Review Fluids* 9, no. 5 (2024): 054605, https://doi.org/10.1103/ PhysRevFluids.9.054605.
- [7] A. Peleg and J. V. Moloney, "Scintillation Index for Two Gaussian Laser Beams With Different Wavelengths in Weak Atmospheric Turbulence," *Journal of the Optical Society of America A* 23, no. 12 (2006): 3114–3122, https://doi.org/ 10.1364/JOSAA.23.003114.
- [8] S. Shao, F. Qin, M. Xu, Q. Liu, Y. Han, and Z. Xu, "Temporal and Spatial Variation of Refractive Index Structure Coefficient Over South China Sea," *Results in Engineering* 9 (2021): 100191, https://doi.org/10.1016/j.rineng.2020.100191.
- [9] R. Z. Tian, H. Y. Xu, Q. L. Dong, and Z. Y. Ye, "Numerical Investigation of Aero-Optical Effects of Flow Past a Flat-Windowed Cylindrical Turret," *Physics of Fluids* 32, no. 5 (2020): https://doi.org/10.1063/1.5144704.
- [10] X. Ren, H. Yu, X. Yao, H. Su, and P. Hu, "Shock Boundary Layer Interaction and Aero-Optical Effects in a Transonic Flow Over Hemisphere-on-Cylinder Turrets," *International Journal of Aerospace Engineering* 2022 (2022): 3397763, https://doi.org/10.1155/2022/3397763.
- [11] H. Schlichting, Boundary-layer theory (McGraw-Hill, 7th edition, 1979).
- [12] S. Gordeyev and E. Jumper, "Fluid Dynamics and Aero-Optics of Turrets," *Progress in Aerospace Sciences* 46, no. 8 (2010): 388–400, https://doi.org/10.1016/j.paerosci.2010.06.001.
- [13] K. P. Lynch, N. E. Miller, D. R. Guildenbecher, L. Butler, and S. Gordeyev, "Aero-Optical Measurements of a Mach 8 Boundary Layer," *AIAA Journal* 61, no. 3 (2023): 991–1001, https://doi.org/10.2514/1.J062363.
- [14] S. Gordeyev and L. Butler, "Aero-Optical Distortions of a Turbulent Boundary Layer at Back-Looking Viewing Angles," AIAA Journal 63, no. 7 (2025): 2635–2643, https://doi.org/10.2514/1.J064880.
- [15] V. M. Canuto, G. J. Hartke, A. Battaglia, J. Chasnov, and G. F. Albrecht, "Theoretical Study of Turbulent Channel Flow: Bulk Properties, Pressure Fluctuations, and Propagation of

- Electromagnetic Waves," *Journal of Fluid Mechanics* 211 (1990): 1–35, https://doi.org/10.1017/S0022112090001471.
- [16] D. Ding, Y. Wang, B. Zhang, and H. Liu, "Aero-Optics of a Three Dimensional Sphere with Real Gas Effects in the Near Space," *Optical Engineering* 61, no. 5 (2022): 055101–055101.
- [17] W. Zhang, L. Ju, W. Fan, et al., "Numerical Simulation and Experimental Study on Guidance Performance of Hypersonic Seeker Under Aerodynamic Optical Transmission Effects," Optics Express 32, no. 22 (2024): 38582–38593, https:// doi.org/10.1364/OE.534122.
- [18] S. Yi, H. Ding, S. Luo, X. Sun, and Z. Xia, "Research Progress on Aero-Optical Effects of Hypersonic Optical Window With Film Cooling," *Light: Science & Applications* 13, no. 1 (2024): 310, https://doi.org/10.1038/s41377-024-01596-x.
- [19] Y. Li, S. Deng, C. Xue, and T. Xiao, "Correction of Aero-Optical Effect With Blow-Suction Control for Hypersonic Vehicles," *Applied Sciences* 14, no. 15 (2024): 6653, https://doi.org/10.3390/app14156653.
- [20] Y. Huang, X. L. Xia, and H. P. Tan, "Temperature Field of Radiative Equilibrium in a Semitransparent Slab With a Linear Refractive Index and Gray Walls," *Journal of Quantitative Spectroscopy and Radiative Transfer* 74, no. 2 (2002): 249–261, https://doi.org/10.1016/S0022-4073(01)00238-2.
- [21] S. Deng, J. Wang, and H. Liu, "Experimental Study of a Bio-Inspired Flapping Wing MAV by Means of Force and PIV Measurements," *Aerospace Science and Technology* 94 (2019): 105382, https://doi.org/10.1016/j.ast.2019.105382.
- [22] S. S. Aleyasin, N. Fathi, M. F. Tachie, P. Vorobieff, and M. Koupriyanov, "Experimental-Numerical Analysis of Turbulent Incompressible Isothermal Jets," in *Fluids Engineering Division Summer Meeting Vol. 58066* (American Society of Mechanical Engineers, 2017), V01CT23A015, https://doi.org/ 10.1115/FEDSM2017-69418.
- [23] S. Gordeyev, J. Cress, A. Smith, and E. Jumper, "Improvement in Optical Environment Over Turrets With Flat Window Using Passive Flow Control," in *Proceedings of the 41st Plasmadynamics and Lasers Conference* (American Institute of Aeronautics and Astronautics Inc. (AIAA), 2010), 4492.